Electrical and electrochemical properties of architectured electrodes based on perovskite and A2MO4-type oxides for Protonic Ceramic Fuel Cell

Pierre Batocchi, Fabrice Mauvy, Sébastien Fourcade, M. Parco

▶ **To cite this version:**

Pierre Batocchi, Fabrice Mauvy, Sébastien Fourcade, M. Parco. Electrical and electrochemical properties of architectured electrodes based on perovskite and A2MO4-type oxides for Protonic Ceramic Fuel Cell. Electrochimica Acta, 2014, 145, pp.1-10. 10.1016/j.electacta.2014.07.001 . hal-01071524

HAL Id: hal-01071524
https://hal.science/hal-01071524

Submitted on 22 Jun 2022

HAL is a multi-disciplinary open access archive for the deposit and dissemination of scientific research documents, whether they are published or not. The documents may come from teaching and research institutions in France or abroad, or from public or private research centers.

L'archive ouverte pluridisciplinaire **HAL**, est destinée au dépôt et à la diffusion de documents scientifiques de niveau recherche, publiés ou non, émanant des établissements d'enseignement et de recherche français ou étrangers, des laboratoires publics ou privés.

Electrical and electrochemical properties of architectured electrodes based on perovskite and A_2MO_4-type oxides for Protonic Ceramic Fuel Cell

P. Batocchi[a], F. Mauvy[a], S. Fourcade[a], M. Parco[b]

[a] *CNRS, Université de Bordeaux, ICMCB, 87 Av. du Dr Schweitzer, F-33608 Pessac Cedex, France*
[b] *Fundación TECNALIA, Research & Innovation 20009 San Sebastian, Spain*

Abstract

Two mixed ionic-electronic conducting oxides (MIEC) have been investigated as potential cathode materials for protonic ceramic fuel cell (PCFC): the perovskite $Ba_{0.5}Sr_{0.5}Co_{0.8}Fe_{0.2}O_{3-\delta}$ (BSCF) and the Ruddlesden Popper $Pr_2NiO_{4+\delta}$ (PrN). Their electrical properties have been studied over a large range of water vapour partial pressure. All compounds exhibit high electronic conductivities ($\sigma \geq 40$ S.cm^{-1} at 600 °C) whatever the pH_2O of the surrounding atmosphere. Electrochemical characterizations have been performed as a function of pH_2O, under zero dc conditions and under dc polarization using symmetrical cells based on $BaCe_{0.9}Y_{0.1}O_{3-\delta}$ (BCY10) as electrolyte. For this purpose, two electrode architectures have been elaborated: a single phase electrode and a composite cathode/BCY10 architectured electrode. All electrodes showed pH_2O-dependence with promising polarization resistance values lower than 0.8 Ω cm^2 at 600 °C under air whatever the gas humidification rate. The use of architectured electrodes led to a significant decrease of the polarization resistance with values as low as 0.23 and 0.19 Ω cm^2 for PrN and BSCF respectively, at 600 °C and pH_2O = 0.20 bar. Concerning the oxygen reduction reaction (ORR) mechanisms, rate determining steps involving protons have been identified. They have been respectively assigned to the proton interface transfer and to the water formation and/or desorption for single phase and architectured electrodes. This change has been attributed to an extent of the electrochemically active area and to an enhancement of the protonic transport properties in the architectured electrodes. However electrodes performances seem to be governed by the dissociative adsorption of oxygen species and/or the charge transfer. Concerning performances under dc current, cathodic polarization is reduced when architectured electrodes are used. An enhancement of the electrodes performances has been also evidenced with water content increasing which corroborates the protonic conduction process into the cathode materials.

1. Introduction

Solid oxide fuel cells (SOFC) are considered as promising alternative power sources due to their high efficiency and low pollution emission. However their commercialization is limited by high operating temperatures (800-1000 °C) which cause accelerated thermal ageing of the materials and high cost of the components. Consequently, great efforts have been devoted to reduce their operating temperature in the 400-600 °C range. Such restriction mainly implies the development of alternative electrolyte and cathode materials able to operate in this intermediate temperature range without any drastic effect on cell performances. Since more than two decades, protonic ceramic fuel cells (PCFC) have been considered as an interesting alternative due to the lower activation energy of the protonic conduction (0.4-0.6 eV) [1] compared to the classical oxygen ion conductors. Iwahara et al. [2-4] first reported protonic conduction in oxygen deficient perovskite oxides such as doped $SrCeO_3$ and $BaCeO_3$ by water incorporation into the structure according to the relation :

$$H_2O_{(g)} + V_O^{\bullet\bullet} + O_O^x \Leftrightarrow 2OH_O^{\bullet} \qquad (1)$$

Since then, acceptor-doped perovskite oxides formulated $AM_{1-x}M'_xO_{3-\delta}$ such as barium cerates are considered as the best protonic conductors but suffer from poor chemical stability under acidic (CO_2) and/or wet atmospheres [5]. In order to enhance stability of these compounds, solid solutions between $BaCeO_3$ and $BaZrO_3$ have been widely investigated [6-8]. However, high conductivity and low reactivity are antagonist properties and so optimisation of compositions is crucial in order to find the best compromise for a PCFC electrolyte application.

Unlike SOFCs, water vapour is formed at the cathode side of a PCFC according to the relation [9]:

$$O_{2(g)} + 4OH_O^{\bullet} + 4e' \Leftrightarrow 2H_2O_{(g)} + 4O_O^x \qquad (2)$$

This specific feature prevents fuel dilution which can lead to a reduction of the cell efficiency in SOFCs, but makes the oxygen reduction reaction (ORR) and the water exhaust management more complex in the PCFC technology. In addition, the lack of proper cathode materials in PCFCs often leads to the use of conventional mixed ionic-electronic (O^{2-}/e^-) conducting oxides (so-called MIEC). Consequently, the triple phase boundary area (TPB) is confined to the electrolyte/electrode interface, leading to large cathodic polarization resistance. To extend the electrochemically active area, a suitable cathode material should possess a mixed H^+/e^- conductivity with a good electrocatalytic activity toward ORR. However up to now, protonic conductors with an electronic conductivity large enough have not been reported [10].

In order to overcome this problem, several approaches have been considered. The most widespread one is to elaborate composite electrodes by mixing electrolyte and cathode materials. In addition to the enlargement of the active sites for the ORR, this approach has the advantages to improve the electrode adherence to the electrolyte and to reduce thermal expansion coefficient (TEC) mismatching between electrolyte and cathode layer. For this purpose, various perovskite-type oxides have been investigated such as $Ba_{0.5}Sr_{0.5}Co_{0.8}Fe_{0.2}O_{3-\delta}$ (BSCF) [11], $La_{0.6}Sr_{0.4}Fe_{0.8}Co_{0.2}O_{3-\delta}$ (LSFC) [12-13] or $Sm_{0.5}Sr_{0.5}CoO_{3-\delta}$ (SSC) [14-18]. Development of efficient composite electrodes requires optimization in terms of composition and elaboration process. Indeed, percolation of both proton conducting and MIEC phases is essential to not affect the electrocatalytic activity of the electrode. Wu et al. [15] studied the influence of the SSC content on the

polarization resistance using composite cathodes based on $BaCe_{0.8}Sm_{0.2}O_{3-\delta}$ (BCS) electrolyte, elaborated by screen-printing. Values decreased with MIEC insertion until a minimum of 0.67 Ω cm^2 at 600 °C at a 60 wt.% content. According to the literature data, it can be considered that a weight ratio between 60 and 70% of cathode material should be enough to create conduction pathways for oxygen ions, protons and electrons and so to reach good electrode performances. Obviously, this ratio depends on the density and particle size of the materials, and on the elaboration process.

Considering that most of MIEC oxides exhibit oxygen non-stoichiometry, an other approach could be to consider a possible mixed $H^+/O^{2-}/e^-$ conduction in wet conditions. For this purpose, recent works [19-20] have investigated electrochemical properties of several perovskite-related compounds under moist atmosphere. The highly oxygen deficient perovskite BSCF showed attractive water insertion abilities with respect to a large amount of vacant sites [20]. On the other hand, over-stoichiometric layered compounds such as Ruddlesden-Popper series $Ln_2NiO_{4+\delta}$ and double perovskites $LnBaCo_2O_{5+\delta}$, have drawn the attention because of their interesting oxygen transport properties with respect to their anisotropic oxygen diffusion and cation ordered structures [21-25]. These oxides exhibit high values of surface exchange and oxygen diffusion coefficients with low activation energies which make them suitable for a PCFC cathode application. Particularly, the $Pr_2NiO_{4+\delta}$ (PrN) composition has been found to be a possible mixed $H^+/O^{2-}/e^-$ conducting oxide with a low polarization resistance when cooperates with a proton conductor (BCY10) [20].

In this work, a combination of these two approaches is proposed in order to reach good electrode performances. Referring to previous results [19], [20], [26], two promising MIEC oxides have been selected as cathode materials: the perovskite $Ba_{0.5}Sr_{0.5}Co_{0.8}Fe_{0.2}O_{3-\delta}$ (BSCF) and the Ruddlesden-Popper $Pr_2NiO_{4+\delta}$ (PrN) with the K_2NiF_4-type structure. As a first step, their electrical properties have been studied over a large range of water partial pressure (pH_2O). In a second step, electrochemical studies under zero dc conditions have been performed in wet air using symmetrical cells with $BaCe_{0.9}Y_{0.1}O_{3-\delta}$ (BCY10) as electrolyte material. For this purpose two electrode architectures have been investigated: a single phase electrode based on pure MIEC oxide, and an architectured one based on composite BCY10-cathode materials. Concerning the architectured electrodes, the goal is not only to improve the mechanical adherence near the electrode/electrolyte interface and to reduce thermal expansion coefficient (TEC) mismatching but also to optimize the electrochemical properties by the help of the microstructure tuning. For each cell, electrochemical properties against the pH_2O have been analysed in terms of polarization resistances and rate-determining steps involved in the ORR mechanisms. Finally, electrochemical measurements under dc polarization have been carried out to study architectured electrodes performances.

2. Experimental

2.1. Structural characterization

Commercial powders provided by the company Marion Technologies were used as electrolyte and cathode materials. The powders were characterized by X-ray diffraction (XRD) at room temperature on a PANalytical X'pert MPD Bragg-Brentano θ-θ geometry diffractometer, over an angular range of 2θ = 8-120°, using Cu-Kα radiation. All materials were found to be single phases and were refined in orthorhombic (BCY10, PrN) or cubic (BSCF) space groups with the FullProf program to obtain the lattice parameters. Results from this work are listed in Table 1 and are in agreement with the literature data [27-29].

Table 1
Lattice parameters of studied materials.

Type of material	Abbreviation	Composition	Space group	Lattice parameters (Å)
Electrolyte	BCY10	$BaCe_{0.9}Y_{0.1}O_{3-\delta}$	Pmcn	a = 8.764(2) b = 6.203(2) c = 6.230(2)
Cathode	PrN	$Pr_2NiO_{4+\delta}$	Bmab	a = 5.4631(5) b = 5.3812(5) c = 12.464(1)
Cathode	BSCF	$Ba_{0.5}Sr_{0.5}Co_{0.8}Fe_{0.2}O_{3-\delta}$	Pm-3 m	a = 4.0013(4)

2.2. Chemical reactivity

From a general point of view, the chemical reactivity between electrolyte and cathode materials is considered as an important issue for the fuel cell performances [10]. Thus, it is well known that a high reactivity can promote the formation of insulating phases at the electrolyte/electrode interface leading to a lowered ionic transfer and consequently to a drastic increase of the polarization resistance. In addition, a poor cathode layer adhesion can have a detrimental effect on the interface area, contributing to increase the polarization resistance and inducing a delamination process.

According to these considerations, the chemical reactivity between BCY10 electrolyte and selected cathode materials has been investigated under sintering conditions. Powders of electrolyte and cathode materials were thoroughly mixed in a (1:1) weight ratio and then pressed into pellets in order to exacerbate the reactivity. The pellets were then fired in air, at 1200 °C and 1100 °C for 1 hour for the PrN-BCY10 and BSCF-BCY10 mixtures, respectively. XRD patterns of powder mixtures before and after heat treatment have been reported in Fig. 1.

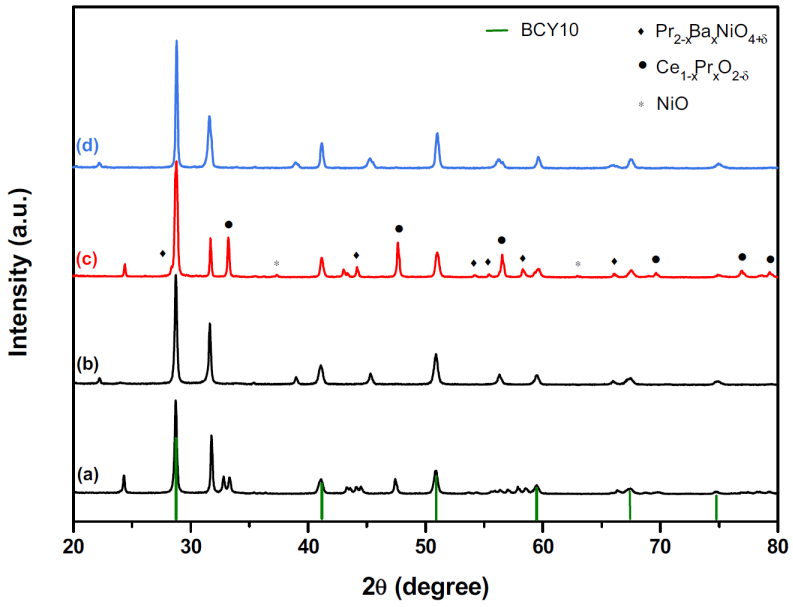

Fig. 1. XRD patterns of PrN-BCY10 (a) and BSCF-BCY10 (b) as-prepared mixtures, and PrN-BCY10 (c) and BSCF-BCY10 (d) after heat treatment.

Results show that BSCF does not obviously react with BCY10 after heat treatment while reaction between electrolyte material and PrN led to the formation of a small amount of secondary phases like $Ce_{1-x}Pr_xO_{2-\delta}$ and NiO. In addition, the presence of a phase-type $Pr_{2-x}Ba_xNiO_{4+\delta}$ suggests possible barium diffusion in the nickelate structure. $Ce_{1-x}Pr_xO_{2-\delta}$ fluorite-type oxides are considered to be mixed ionic-electronic conductors and have been previously investigated as potential active layers in SOFCs [30]. Thus, it can be supposed in this work that the

formation of such a phase is not detrimental to the ORR and in addition, could promote the electrode adherence to the electrolyte. Similarly a limited diffusion of barium into the nickelate structure ($x \leq 0.3$) should not significantly affect electrochemical properties of the electrode [31].

2.3. Preparation of dense ceramics

In order to perform electrical and electrochemical measurements described below, ceramics with compacities higher than 94% are required to avoid the presence of open porosity [32]. For this purpose, fine powders with a small particle size ($D_v(0.5)$ ≈ 0.40 µm for all compositions) as well as optimized shaping and thermal treatments remain basic conditions.

For the cathode materials, powders were ground using an agate mortar and isostatically pressed into pellets (20 mm diameter, 1-2 mm thick) at 3000 bars for 5 min. The pellets were then sintered in air at 1350 °C for 4 hours and 1200 °C for 12 hours respectively for PrN and BSCF. After sintering, they were manually polished with a 4000 grade SiC paper in order to get mirror surfaces. The densities of the as-prepared ceramics were determined by the geometric method and were higher than 95% of the theoretical values.

In the case of electrolyte ceramics, BCY10 powder was in the same way isostatically pressed at 3000 bars for 5 min into 20 mm diameter pellets and then sintered in air at 1400 °C for 10 hours. The surface of the pellets was finally roughened with a 600 grade SiC paper to get uniform surface conditions. All the sintered BCY10 ceramics have a diameter of ≈ 15.5 mm, a thickness of ≈ 1 mm and a densification rate upper than 95%.

2.4. Elaboration of symmetrical cells

In order to study different architectured electrodes, two symmetrical cells have been elaborated as described in Fig. 2. The first one, named single phase electrode, consists of a two-layer deposition of the cathode material, while the so-called architectured electrode is made of a composite BCY10-cathode interface layer associated with a single phase top layer. In the second configuration, the composite interface layer is expected to increase the protonic conductivity in the cathode and to enhance both ionic transfer and mechanical compatibility (adhesion, TEC) at the electrolyte/electrode interface as demonstrated in the litterature [13], [15], [33]. Finally, a single phase top layer is added to ensure a good current-collection. In order to get homogeneous composite electrodes, electrolyte and cathode powders have been thoroughly mixed in a (3:7) weight ratio into a mortar and then ball-milled at 500 rpm for 1 hour.

Screen-printing method was selected for the electrodes deposition. Inks were first elaborated by mixing cathode materials powders into a solvent with dispersant (terpineol) and binder (ethylcellulose) commercial agents. The ink formulation has been optimized both in terms of particle size distribution and composition [34]. Before deposition, a three-cylinder grinding step was done to avoid powder agglomeration and to ensure homogeneous inks. Electrodes were then screen-printed on both sides of dense BCY10 pellets and sintered in air for 1 hour at 1100 °C for BSCF single phase and architectured BSCF-BCY10 electrodes, and at 1170 and 1200 °C for PrN single phase and PrN-BCY10 architectured electrodes respectively. The sintering conditions have been optimized to get porous cathodes without excessive reactivity between materials, while keeping a good

adhesion to the electrolyte pellet. An initial ramp of 1 °C min^{-1} up to 400 °C is used to eliminate organic binders, followed by a heating rate of 3 °C min^{-1} up to the sintering temperature.

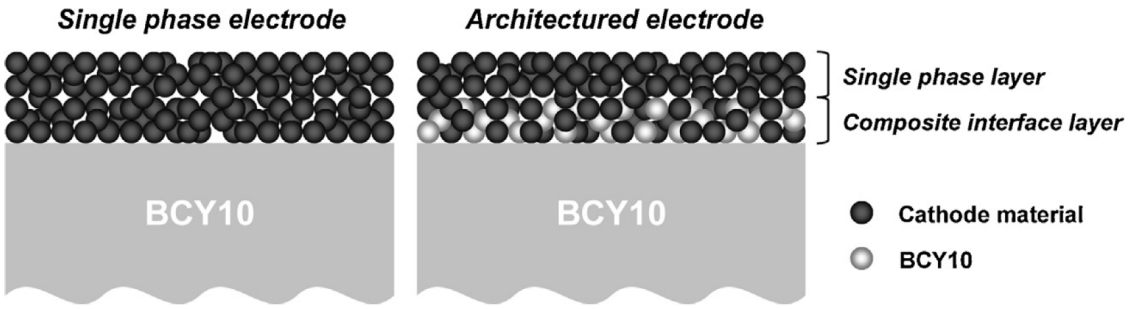

Fig. 2. Schematic representation of the two symmetrical cell configurations tested in this study.

After sintering, the electrodes microstructure was observed by field emission scanning electron microscopy (SEM) using a JEOL JSM 6330F equipped with an energy dispersive spectrometer (EDS) detector. Micrographs of PrN-based symmetrical cells are given as an example in Fig. 3. From cross-section views, a good adherence of the electrodes has been evidenced with an average thickness of about 30 µm. Foremost, homogeneous microstructures were found in any cases with a fine distribution of grain size and pore volume. However coarser particles have been observed for single phase layers, with a mean size around 1 µm, against 0.5 µm for the composite ones. The porosity has been calculated from image analysis using Image J software, and is close to 30 and 20% for the single phase and the composite layers respectively. Such porosity levels can be considered high enough for gas diffusion and water vapour exhaust.

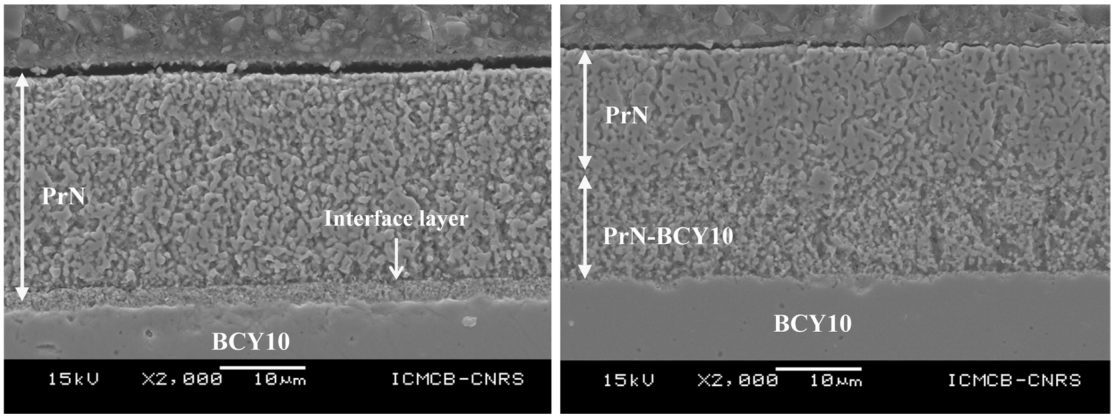

Fig. 3. Typical SEM micrographs of the elaborated symmetrical cells after sintering: BCY10/PrN single phase (a), BCY10/PrN architectured (b) as an example.

Otherwise, one can note the presence of an interface layer for the PrN single phase symmetrical cells, which was identified as a cerium-rich phase $Ce_{1-x}Pr_xO_{2-\delta}$-type by EDS analysis. This result confirms the reactivity of the nickelate with the BCY10 electrolyte previously highlighted with XRD measurements. However the impact of this interface layer on the electrochemical performances has not been identified [20], [26] in so far as this ceria based compound seems to be a good ionic conductor and to enhance the electrode adherence. It can be noticed that this phase does not appear in the case of the architectured electrode.

2.5. Electrochemical measurements

The polarization resistance and overpotential versus current density curves of the as-prepared electrodes were determined by electrochemical impedance spectroscopy (EIS) and voltamperometry measurements. Measurements were performed either in two-electrode configuration (under zero dc conditions) or in three-electrode configuration (under dc polarization) as depicted in Fig. 4. For the three-electrode configuration (Fig. 4b), a specific cell-design was adopted: working and counter electrodes were screen-printed on both sides of the electrolyte pellet in a symmetrical way, covering the half area of the ceramic. A platinum electrode was then painted on the same side of the working electrode, at a distance larger than five times the electrolyte thickness in order to reduce the current lines interactions [35-37].

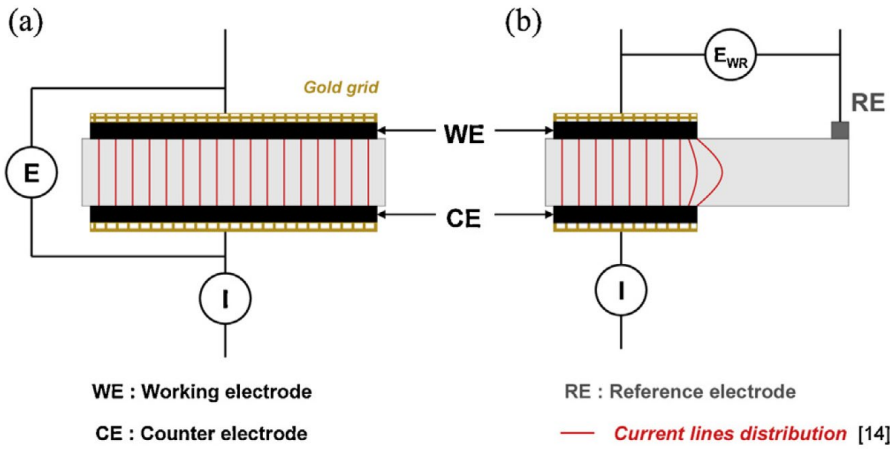

Fig. 4. Schematic representation of the two-electrode (a) and three-electrode (b) configurations used for EIS measurements.

EIS measurements were achieved with an Autolab PGSTAT 30 equipped with a frequency response analyzer (FRA), in the range of 0.01 Hz to 1 MHz applying 50 mV signal amplitude. Gas humidification rate was adjusted in the range $0.03 \leq pH_2O \leq 0.30$ bars, by bubbling air into a water tank heated at a given temperature. Measurements were carried out with respect to an equilibrium time of about 2 hours and during heating and cooling thermal cycles. Impedance diagrams were fitted using Zview™ software (Scribner Associates).

3. Results and discussion

3.1. Electrical measurements

The total electrical conductivity of the cathode materials was determined by the direct current four-probe method on dense pellets [38-39]. Measurements were performed under air, in the temperature range 100–700 °C and over a large range of water partial pressure (0.10–0.30 bars). Electrical conductivity has been reported in Fig. 5 as a function of the inverse temperature, for cooling and heating cycles. Both phases exhibit semi-conducting type behaviour: electronic conductivity is increasing until 500-550 °C, and then slightly decreases due to the loss of oxygen in structures and consequently to the diminution of the charge carriers density as evidenced in previous studies [19], [22], [40]. In addition, an hysteresis was observed for BSCF curves until 600 °C resulting from an oxygen stoichiometry variation during cooling and heating cycles, previously reported by thermogravimetric analyses [19-20].

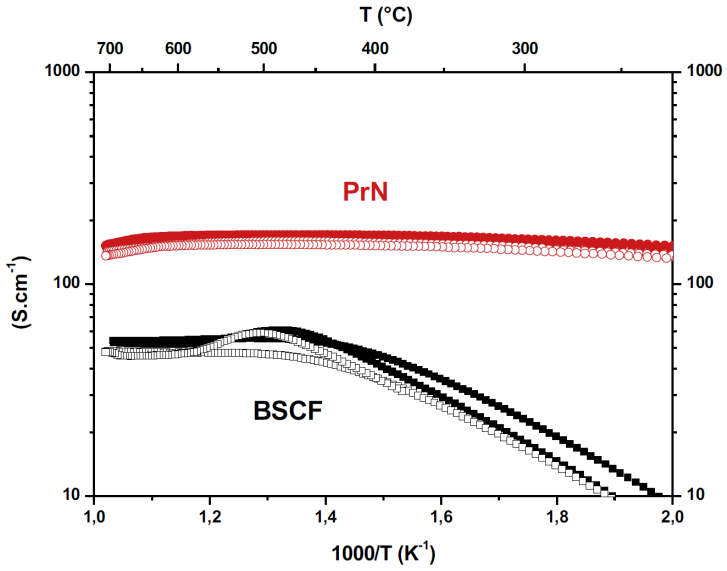

Fig. 5. Thermal variation of the electrical conductivity under dry (full symbols) and humidified-0.30 bar H_2O (open symbols) air.

From data analysis, conductivity of PrN was found to be approximately three times higher than the BSCF one, with values reaching respectively 167 and 54 S cm^{-1} at 600 °C under dry atmosphere. Furthermore, water steam introduction did not significantly affect electrical properties as shown by the conductivities measured under high humidification rates (0.30 bar H_2O), resulting in 153 and 47 S cm^{-1} at 600 °C for PrN and BSCF compounds, respectively.

These results suggest that expected hydroxyle species formation inside the structures due to water insertion [19-20] does not modify the concentration of holes and so electrical properties of these compounds remain unchanged. Moreover, these materials exhibit an electrical conductivity higher than 40 S cm^{-1} at 600 °C whatever the pH_2O, which makes them suitable for application in a fuel cell.

3.2. Electrochemical measurements under zero dc conditions

EIS measurements were performed under zero dc conditions i.e. at thermodynamical equilibrium, as a function of temperature and water partial pressure. From a general point of view, impedance diagrams show several contributions which can be assigned to specific phenomena. A typical Nyquist plot recorded at 600 °C under wet air (0.20 bar H_2O) for a BCY10/PrN symmetrical cell is reported in Fig. 6a. Referring to previous studies [19], [20], [41], experimental data were fitted using equivalent circuits constituted of a series resistance (R_s) and resistance-constant phase elements (R-CPE) in parallel associated in series. In the high frequency (HF) range, the electrolyte response can be modelled in most diagrams, by a series resistance whose value is in agreement with the protonic conductivity of the BCY10 in wet atmosphere (~ 10^{-2} S cm^{-1} at 600 °C) [42-44]. The two depressed semi-circles observed in the middle (MF) and low (LF) frequency ranges corresponds to the electrode response and have been fitted using two R-CPE elements. Polarization resistance (R_p) is calculated using the following formula:

$$R_p = \frac{(R_{MF} + R_{LF}) \times A}{2} \qquad (3)$$

where R_{MF} and R_{LF} are the polarization resistances of MF and LF contributions respectively, and A the electrode surface area.

From fitted data, equivalent capacitances (C_{eq}) and relaxation frequencies (f_{relax}) of each contribution have been determined using relations (4) and (5) [19].

$$C_{eq} = R^{\left(\frac{1-p}{p}\right)} \times CPE^{\frac{1}{p}} \quad (4)$$

$$f_{relax} = \frac{1}{2\pi(R \times CPE)^{1/p}} \quad (5)$$

where p is a parameter used to compensate for non-homogeneity in the system (with a value between 0.9 and 1).

Calculated values have been systematically plotted as a function of the temperature, in the Schouler-type representation, which can be considered as a reference for interpreting an experimental impedance diagram [45]. Results obtained for the PrN single phase electrode are reported in Fig. 6b and 6c.

With respect to equivalent capacitance and relaxation frequency values, two electrochemical processes can be distinguished. Constant capacitances and a linear temperature dependence of the associated frequencies indicate also that involved phenomena seem to remain the same all over the studied temperature range. The middle-frequency contribution (10^3–10^5 Hz) is characterized by low capacitance values, approximately 10^{-5} F. According to previous results, the related electrochemical process could be interpreted as the electrolyte/electrode interface ionic transfer [19], [41]. The low frequency contribution (0.01–10 Hz) which is defined by higher capacitance values (~ 10^{-1} F), could be assigned to the charge transfer and to the electrode reaction process.

While quite similar results have been found for the BCY10/BSCF symmetrical cell, differences were highlighted in the case of the architectured ones. More precisely, higher capacitance values (~ 10^{-2} F) and a lower frequency range (10^1–10^3 Hz) were obtained for the MF contribution. Such a difference could be explained by an improvement of the electrolyte/cathode ionic transfer due to the composite interface layer. Otherwise, no differences were found regarding the LF contribution, suggesting that the involved process is similar.

Thermal variation of the MF and LF resistances has been investigated. Results obtained for the PrN single phase electrode are shown in Fig. 6d. On the whole, R_{MF} and R_{LF} decrease with increasing temperature due to the thermal activation of the related electrochemical reactions. Concerning single phase electrodes, the simulated activation energies of R_{MF} are around 0.6 eV which are closed to the values reported for proton conductivity in BCY10 under wet air [42], [46]. This implies that the associated electrochemical process might involve protons, which is consistent with the interface ionic transfer assumption. In any cases, the low-frequency contribution exhibits the highest resistance and activation energy values, suggesting that electrode reaction might be the rate-limiting step.

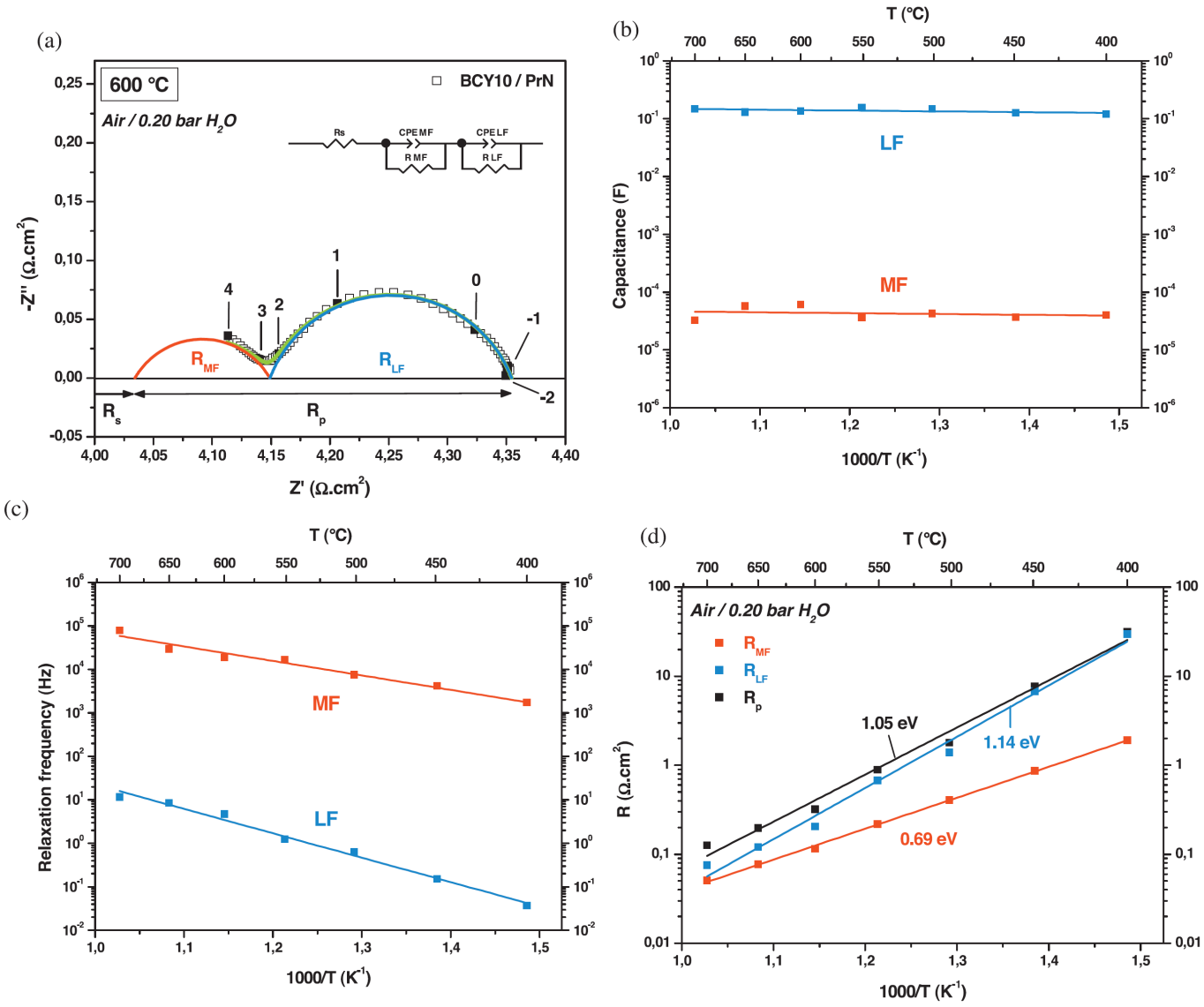

Fig. 6. Typical impedance diagram obtained at 600 °C (a), thermal variation of capacitances (b) and relaxation frequencies (c) of the identified middle and low frequency phenomena and Arrhenius plots of the total, middle and low frequency resistances (d) under wet air (0.20 bar H_2O) for BCY10/PrN symmetrical cell.

3.3. Comparison of the electrochemical performances of single phase and architectured electrodes at fixed pH_2O (0.20 bar)

Arrhenius plots of the polarization resistances of PrN and BSCF single phase electrodes are reported in Fig. 7a. Despite higher activation energy, PrN electrode exhibits the lowest polarization resistance for temperatures above 500 °C. Corresponding values reach respectively 0.32 and 0.60 Ω cm^2 for PrN and BSCF electrodes at 600 °C, which are significantly lower than those reported in previous works [26], [47], [48].

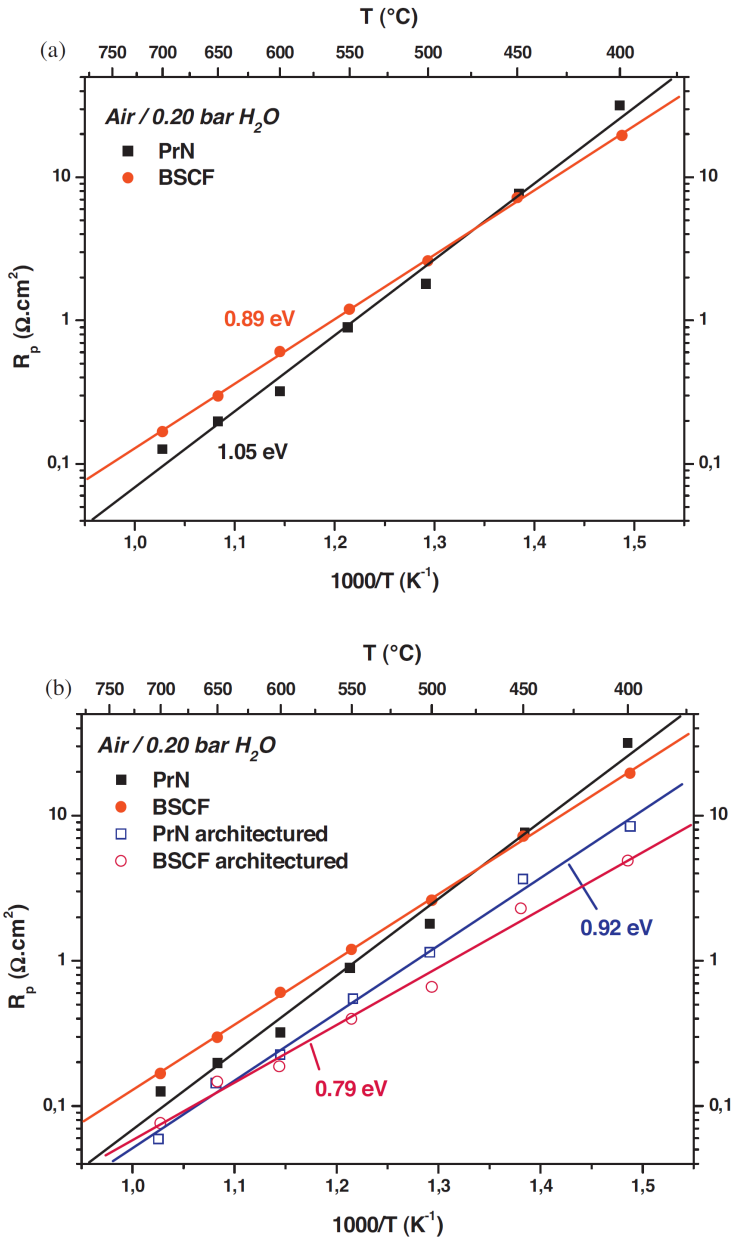

Fig. 7. Arrhenius plots of the polarization resistances for single phase (a) and architectured (b) PrN and BSCF electrodes under wet air (0.20 bar H_2O).

When using architectured electrodes (Fig. 7b), polarization resistances and activation energies significantly decrease. Comparatively, BSCF-based electrode shows better performances than the PrN one with R_p values of 0.19 and 0.23 Ω cm^2 respectively, at 600 °C. Overall, these results demonstrate the significant gain on electrochemical performances when electrode microstructure is optimized.

3.4. Influence of the water partial pressure on the electrochemical properties

In order to study the influence of the water partial pressure on the electrochemical properties, the variation of the polarization resistance has been investigated over a large range of pH_2O (0.03–0.30 bars). Fig. 8 shows the results obtained under air at 600 °C. All cathodes exhibit pH_2O-dependence and whatever the gas humidification rate, promising R_p values < 0.8 Ω cm^2 have been obtained.

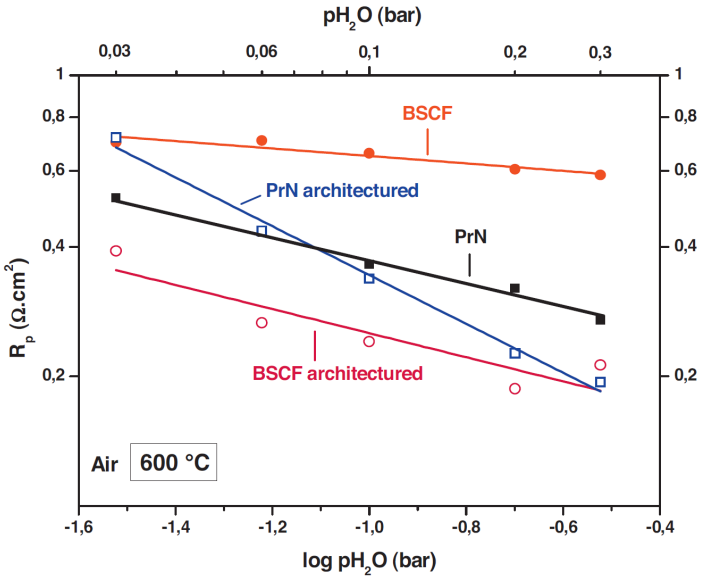

Fig. 8. Polarization resistances variations as a function of water partial pressure at 600 °C.

Because of water formation at the cathode side, the oxygen reduction reaction is assumed to be more complex in PCFCs than in SOFCs. Using platinum electrode as PCFC cathode, Uchida et al. [49] proposed at first the elementary steps involved in the ORR, by adding the formation and evolution of water to the dissociative adsorption and diffusion of oxygen species. Since then, many works have been dedicated to the description of the ORR mechanisms in cathodes based on MIEC O^{2-}/e^{-} oxides [9], [16], [33], [48]. Various models have been suggested including additional reactions related to the transfer and reaction of protons and implying a variable number of elementary steps. The polarization resistance of each of these steps depends on the oxygen and/or water vapour partial pressures, and can be expressed as follow:

$$R_i \propto pO_2^{-m_i} \times pH_2O^{-n_i} \qquad (6)$$

where R_i is the polarization resistance related to the step i, and m_i and n_i the corresponding reaction orders with respect to pO_2 and pH_2O respectively.

With respect to the scheme proposed by Grimaud et al. [20], the oxygen reduction reaction at a PCFC cathode can be decomposed into six elementary steps which are listed in Table 2 with their respective reaction orders. These elementary steps include the adsorption of oxygen gas on the electrode surface (step 1) and the oxygen molecular dissociation (step 2), followed by the oxygen diffusion with charge transfer reaction (step 3). Then, the proton transfer from the electrolyte to the cathode is described by the step 4. Finally the water formation and desorption are defined by steps 5 and 6 respectively.

Table 2
Elementary steps of the oxygen reduction reaction at a PCFC cathode and their reaction order with respect to pO_2 (m) and pH_2O (n) [20].

Step		Elementary reaction	m	n
1	Oxygen adsorption	$O_{(2(g)} \Leftrightarrow O_{2(ads)}$	1	0
2	Oxygen dissociation	$O_{(2(ads)} \Leftrightarrow 2O_{(ads)}$	1/2	0
3	Charge transfer	$O_{(ads)} + 2e' + V_O^{\bullet\bullet} \Leftrightarrow O^x_{O(cathode)}$	1/4	0
4	Proton transfer	$OH^{\bullet}_{O(electrolyte)} + O^x_{O(cathode)} \Leftrightarrow OH^{\bullet}_{O(cathode)} + O^x_{O(electrolyte)}$	0	1/2
5	Water formation	$2OH^{\bullet}_{O(cathode)} \Leftrightarrow H_2O_{(ads)} + V_O^{\bullet\bullet} + O^x_{O(cathode)}$	0	1
6	Water desorption	$H_2O_{(ads)} \Leftrightarrow H_2O_{(g)}$	0	1

To go further into the interpretation of the electrochemical processes previously evidenced, the variation of the polarization resistance versus water partial pressure has been investigated at reduced temperature (450 °C) in order to better identify the different contributions of the impedance diagrams. As EIS measurements were achieved under air, only the pH_2O influence has been studied, considering that the oxygen partial pressure did not vary significantly ($pO_2 \sim 0.21$ bar).

Impedance diagrams recorded for the architectured PrN electrode are reported in Fig. 9. In order to simplify the comparison the ohmic drop, related to the electrolyte contribution, has been subtracted. As seen in Fig. 8, it can be noticed a notable reduction of the polarization resistance when water partial pressure is increasing with values starting from 6.81 Ω cm^2 at 0.03 bar to 2.88 Ω cm^2 at 0.30 bar of steam water.

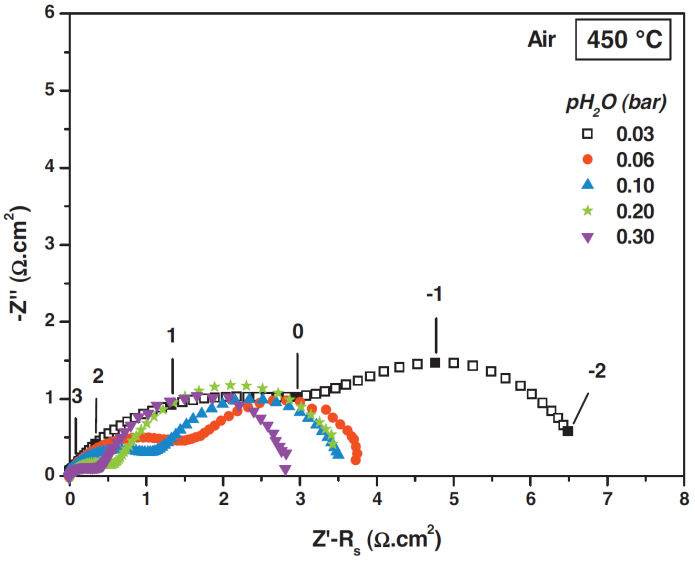

Fig. 9. Impedance diagrams recorded at 450 °C in the water partial pressure range 0.03-0.30 bar, for the architectured PrN electrode.

Variations of the MF and LF capacitances, relaxation frequencies and resistances have been studied in more details. Corresponding values obtained at the same temperature for the PrN-based electrodes are given as an example in Fig. 10. According to Fig. 10a, constant capacitance values were found versus water partial pressure indicating that the associated electrode phenomena remain the same over the whole pH_2O range. These results indicate that there are no significant changes in the cathode materials composition and in the ionic transport properties. It can be added that a good mechanical strength of the electrodes and interfaces microstructures is obtained, even at high water content. As described before, the MF contribution of the architectured electrode shows higher capacitance and lower frequency values (Fig. 10b) probably due to a modification in the electrochemical process.

(a)

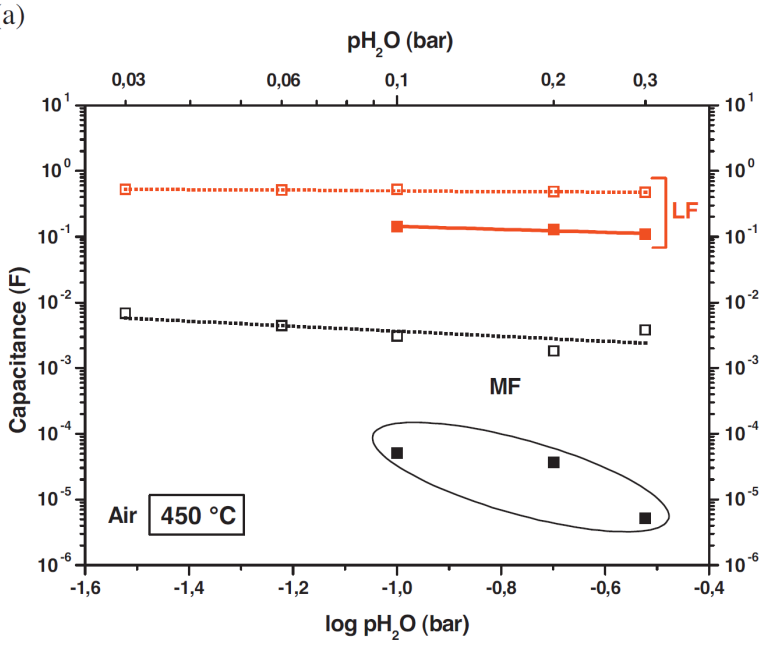
pH2O (bar)
0,03
0,06
0,1
0,2
0,3
Capacitance (F)
LF
MF
Air
450 °C
log pH2O (bar)

(b)

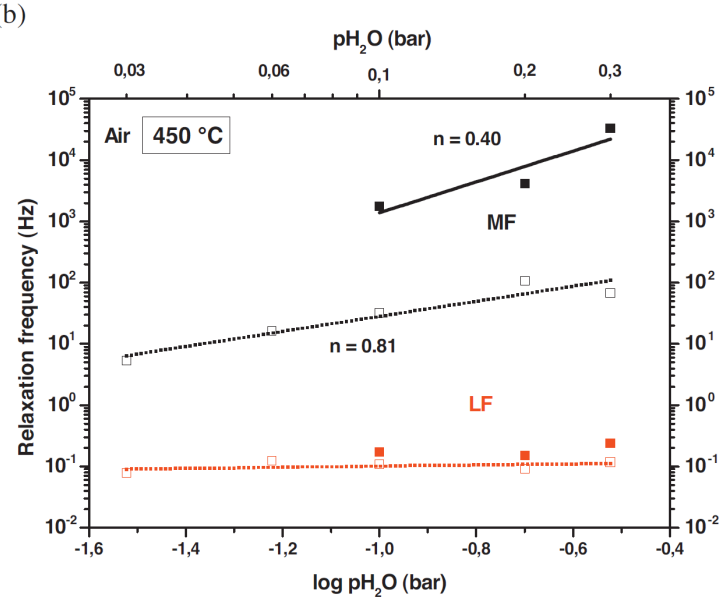
pH2O (bar)
0,03
0,06
0,1
0,2
0,3
Relaxation frequency (Hz)
Air
450 °C
n = 0.40
MF
n = 0.81
LF
log pH2O (bar)

(c)

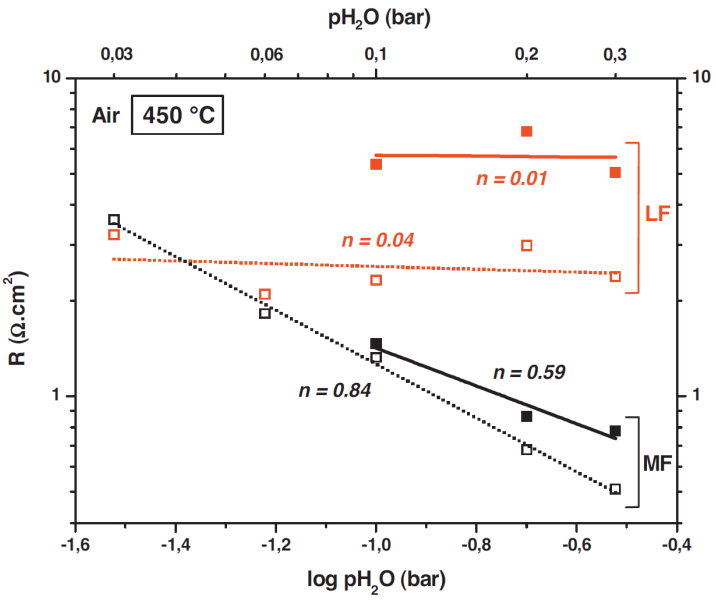
pH2O (bar)
0,03
0,06
0,1
0,2
0,3
R (Ω.cm2)
Air
450 °C
n = 0.01
LF
n = 0.04
n = 0.59
n = 0.84
MF
log pH2O (bar)

Fig. 10. Variations as a function of pH_2O at 450 °C, of MF and LF capacitances (a), relaxation frequencies (b) and resistances (c) for single phase (■) and architectured (□) PrN electrodes.

Concerning MF polarization resistance, one can observe a $pH_2O^{-1/2}$ dependence for the PrN single phase electrode (Fig. 10c), suggesting that the associated rate determining step can be assigned to the proton transfer at the electrolyte/electrode interface (step 4). This result is consistent with the activation energy of R_{MF} (0.6 eV), closed to the BCY10 conductivity. Focusing on the PrN architectured electrode, a pH_2O^{-1} dependence is nearly observed, indicating that the rate determining step is more related to the water formation (step 5) or desorption (step 6). In addition, linear variations of the MF frequencies reported in Fig. 10b are in agreement with the calculated reaction orders. For BSCF-based electrodes, pH_2O dependences were evidenced for R_{MF} but related changes could not be correlated to specific reaction orders.

For both electrodes, the LF contribution seems to be associated to the same process with respect to capacitances and relaxation frequencies and does not depend on pH_2O. So, the associated elementary reaction could be assigned to the oxygen dissociative adsorption or to the charge transfer (step 1-3). In addition, the electrodes performances seem to be governed by the low frequency contribution which exhibits in any cases the highest resistance values. Similar results have been obtained for the BSCF-based electrodes.

On the whole, performances of single phase and architectured electrodes are significantly promoted by the gas hydration rate in the temperature range studied. Concerning the MF contribution, the rate determining step seems to be the proton interface transfer in the case of single phase electrodes while for architectured electrodes, it can rather be assigned to the water formation/desorption. These results suggest firstly a possible protonic conduction in the MIEC phases and secondly an enhancement of the protonic transport properties into the electrodes when composite interface layers are used. On the other hand, with respect to the LF contribution features, the main part of the polarization resistance can be attributed to elementary reactions involving oxygen species. It can be concluded that even if a protonic conduction appears in the BSCF and PrN phases, it should be limited, considering that these oxides are predominantly mixed O^{2-}/e^- conductors.

3.5. Electrochemical measurements under dc polarization

Cathodic overpotential versus current density curves of the architectured electrodes were determined by EIS measurements under dc polarization using the three-electrode configuration described before (Fig. 4b). Impedance diagrams were recorded over a defined dc potential range ($0 \leq E_{WR} \leq 1.5$ V) applied between working and reference electrodes. The resulting cathodic overpotentials (η_{cath}) were calculated as follow:

$$\eta_{cath} = E_{WR} - R_s \times i_{dc} \qquad (7)$$

where R_s (Ω cm^2) is the ohmic drop across the electrolyte measured by EIS and i_{dc} (A cm^{-2}), the resulting current density. Fig. 11 shows the polarization curves of architectured electrodes under wet air at 600 °C. Referring to the work of Grimaud et al. [20], comparison has been made with results obtained on cells based on PrN and BSCF single phase cathode materials associated with BCY10 electrolyte.

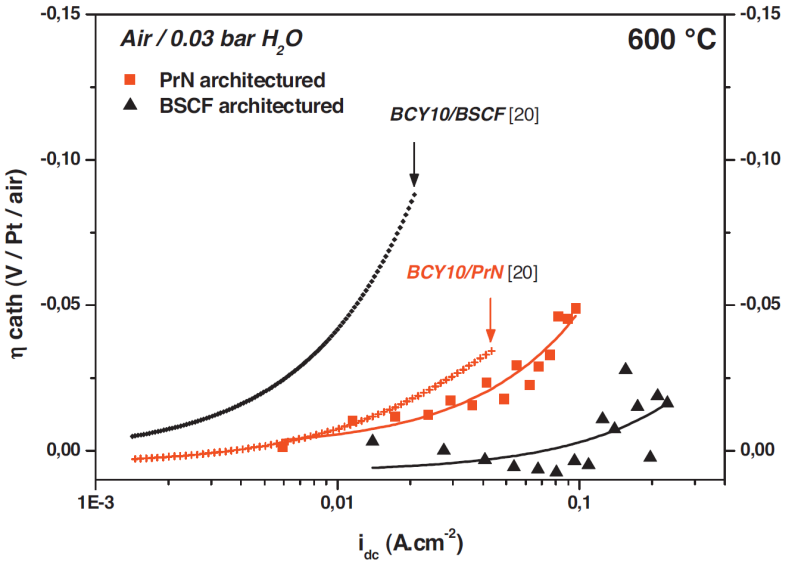

Fig. 11. Cathodic overpotential vs. i_{dc} under wet air (0.03 bar H_2O) at 600 °C for PrN and BSCF-based electrodes.

From polarization curves analysis, it can be seen a large gain on cathodic overpotential when using optimized electrodes. On the one hand, as seen for EIS measurements under zero dc conditions, PrN single phase led to the best performances in the quoted study [20]. On the other hand, when architectured electrodes are used, the BSCF one exhibits the lowest overpotential. In this case positive overpotential values can be obtained for current densities lower than 0.1 A cm^{-2}. Such behaviour is due to the close values of ohmic losses ($R_s \times i_{dc}$) and applied potential (E_{WR}). It can be deduced that good electrochemical performances have been reached. From polarization curves, apparent current exchange densities i_0 have been estimated around 22 mA cm^{-2} for PrN and upper than 100 mA cm^{-2} for BSCF architectured electrodes at 600 °C under wet air. These values are significantly larger than those reported by Dailly at al. [26] for single phase PrN and BSCF cathodes in the same conditions, 8.1 and 6.5 mA cm^{-2} respectively.

In addition, the influence of the water vapour partial pressure has been investigated. For both electrodes, cathodic overpotential clearly decreases with increasing water content, as illustrated in the case of the PrN architectured electrode (Fig. 12). For a given current density of 0.07 A cm^{-2}, measured η_{cath} values reach -0.029, -0.017 and -0.009 V for 0.03, 0.15 and 0.25 bar of steam water, respectively. It can be concluded that high water partial pressures promote electrodes performances as previously evidenced, suggesting a protonic conduction process in the electrode materials.

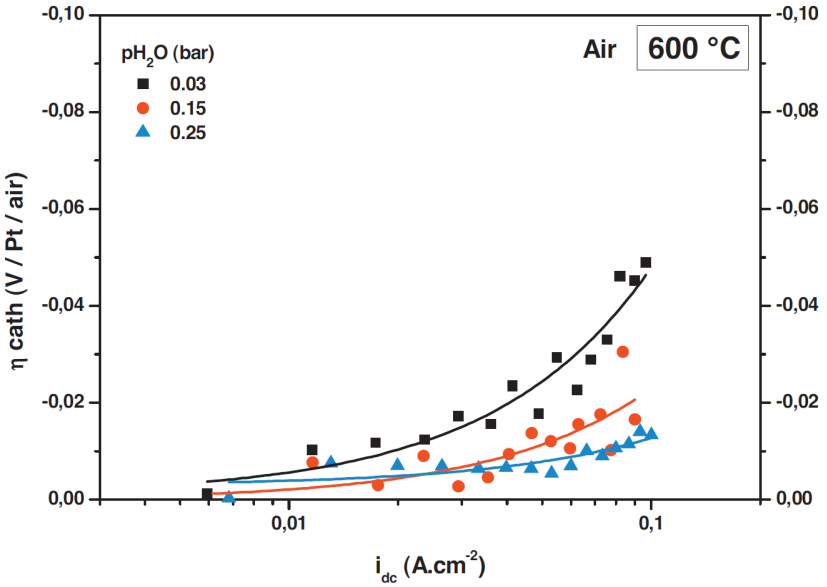

Fig. 12. Cathodic overpotential vs. i_{dc} as a function of pH_2O at 600 °C for PrN architectured electrode.

4. Conclusion

On the basis of previous studies, two promising MIEC oxides have been selected as cathode materials for PCFC application: the perovskite $Ba_{0.5}Sr_{0.5}Co_{0.8}Fe_{0.2}O_{3-\delta}$ (BSCF) and the Ruddlesden Popper $Pr_2NiO_{4+\delta}$ (PrN). Chemical reactivity in sintering conditions with the reference $BaCe_{0.9}Y_{0.1}O_{3-\delta}$ (BCY10) electrolyte material revealed that BSCF was stable while small amount of secondary phases has been evidenced for PrN. Electrical conductivity of the selected materials was investigated as a function of water vapour partial pressure. Steam introduction did not affect the electrical conductivity and compositions kept values higher than 40 S cm^{-1} at 600 °C.

Electrochemical characterizations were performed on symmetrical cells BCY10/cathode elaborated by screen-printing. Two electrode architectures have been elaborated: a so-called single phase electrode, consisting of pure cathode material, and an architectured one, including a composite interface layer. Electrochemical measurements were carried out over a large range of pH_2O under zero dc conditions and under dc polarization. PrN single phase electrode exhibited the lowest polarization resistance with 0.32 Ω cm^2 at 600 °C under wet air (0.20 bar H_2O), against 0.60 Ω cm^2 for BSCF. A large decrease has been obtained using architectured electrodes with values as low as 0.23 and 0.19 Ω cm^2, for PrN and BSCF, respectively tested under the same conditions.

The characterization of electrochemical properties as a function of water vapour partial pressure revealed that all cathodes showed pH_2O-dependence. Even if electrodes performances seem to be governed by the dissociative adsorption of oxygen species and/or the charge transfer, a proton conduction mechanism can be supposed for both MIEC phases. In addition, the use of composite architectured electrodes led to an improvement of the protonic transport properties into the cathodes and consequently to an extent of the electrochemically active area. Concerning performances under dc current, the same conclusion can be done as so far as cathodic polarization is reduced when architectured electrodes are used and when increasing water content.

Acknowledgments

The research leading to these results has received funding from the European Community's Seventh Framework Programme (FP7/2011-2014) for the Fuel Cells and Hydrogen Joint Technology Initiative under grant agreement METPROCELL n°277916.

References

[1] K.D. Kreuer. **Proton-Conducting Oxides.** Annual Review of Materials Research, 33 (2003), pp. 333-359.

[2] H. Iwahara, *et al.* **Proton conduction in sintered oxides and its application to steam electrolysis for hydrogen production.** Solid State Ionics, 3-4 (1981), pp. 359-363.

[3] H. Uchida, N. Maeda, H. Iwahara. **Relation between proton and hole conduction in $SrCeO^3$-based solid electrolytes under water-containing atmospheres at high temperatures.** Solid State Ionics, 11 (2) (1983), pp. 117-124.

[4] H. Iwahara, *et al.* **Proton Conduction in Sintered Oxides Based on $BaCeO^3$.** Journal of The Electrochemical Society, 135 (2) (1988), pp. 529-533.

[5] H. Matsumoto, *et al.* **Relation Between Electrical Conductivity and Chemical Stability of $BaCeO_3$-Based Proton Conductors with Different Trivalent Dopants.** Electrochemical and Solid-State Letters, 10 (4) (2007), pp. B77-B80.

[6] K.H. Ryu, S.M. Haile. **Chemical stability and proton conductivity of doped $BaCeO_3$-$BaZrO_3$ solid solutions.** Solid State Ionics, 125 (1–4) (1999), pp. 355-367.

[7] K. Katahira, *et al.* **Protonic conduction in Zr-substituted $BaCeO_3$.** Solid State Ionics, 138 (1–2) (2000), pp. 91-98.

[8] Y. Guo, *et al.* **Zirconium doping effect on the performance of proton-conducting $BaZr_yCe_{0.8-y}Y_{0.2}O_{3-\delta}$ ($0.0 \le y \le 0.8$) for fuel cell applications.** Journal of Power Sources, 193 (2) (2009), pp. 400-407.

[9] R. Peng, *et al.* **Cathode processes and materials for solid oxide fuel cells with proton conductors as electrolytes.** Journal of Materials Chemistry, 20 (30) (2010), pp. 6218-6225.

[10] E. Fabbri, D. Pergolesi, E. Traversa. **Electrode materials: a challenge for the exploitation of protonic solid oxide fuel cells.** Science and Technology of Advanced Materials, 11 (4) (2010), p. 044301.

[11] B. Lin, *et al.* **Intermediate-to-low temperature protonic ceramic membrane fuel cells with $Ba_{0.5}Sr_{0.5}Co_{0.8}Fe_{0.2}O_{3-\delta}$ idem for $BaZ_{0.1}Ce_{0.7}Y_{0.2}O_{3-\delta}$ composite cathode.** Journal of Power Sources, 186 (1) (2009), pp. 58-61.

[12] E. Fabbri, *et al.* **Composite Cathodes for Proton Conducting Electrolytes.** Fuel Cells, 9 (2) (2009), pp. 128-138.

[13] L. Yang, *et al.* **A mixed proton, oxygen ion, and electron conducting cathode for SOFCs based on oxide proton conductors.** Journal of Power Sources, 195 (2) (2010), pp. 471-474.

[14] L. Yang, *et al.* **A Novel Composite Cathode for Low-Temperature SOFCs Based on Oxide Proton Conductors.** Advanced Materials, 20 (17) (2008), pp. 3280-3283.

[15] T. Wu, R. Peng, C. Xia. **$Sm_{0.5}Sr_{0.5}CoO_{3-\delta}$–$BaCe_{0.8}Sm_{0.2}O_{3-\delta}$ composite cathodes for proton-conducting solid oxide fuel cells.** Solid State Ionics, 179 (27–32) (2008), pp. 1505-1508.

[16] F. He, *et al.* **Cathode reaction models and performance analysis of $Sm_{0.5}Sr_{0.5}CoO_{3-\delta}$–$BaCe_{0.8}Sm_{0.2}O_{3-\delta}$ composite cathode for solid oxide fuel cells with proton conducting electrolyte.** Journal of Power Sources, 194 (1) (2009), pp. 263-268.

[17] L. Yang, C. Zuo, M. Liu. **High-performance anode-supported Solid Oxide Fuel Cells based on $Ba(Zr_{0.1}Ce_{0.7}Y_{0.2})O_{3-\delta}$ (BZCY) fabricated by a modified co-pressing process.** Journal of Power Sources, 195 (7) (2010), pp. 1845-1848.

[18] T. Wu, *et al.* **Nano-sized $Sm_{0.5}Sr_{0.5}CoO_{3-\delta}$ as the cathode for solid oxide fuel cells with proton-conducting electrolytes of $BaCe_{0.8}Sm_{0.2}O_{2.9}$.** Electrochimica Acta,, 54 (21) (2009), pp. 4888-4892

[19] J. Dailly, *et al.* **Perovskite and A_2MO_4-type oxides as new cathode materials for protonic solid oxide fuel cells.** Electrochimica Acta,, 55 (20) (2010), pp. 5847-5853.

[20] A. Grimaud, *et al.* **Hydration Properties and Rate Determining Steps of the Oxygen Reduction Reaction of Perovskite-Related Oxides as H^+ -SOFC Cathodes.** Journal of The Electrochemical Society, 159 (6) (2012), pp. B683-B694.

[21] J.M. Bassat, *et al.* **Anisotropic ionic transport properties in $La_2NiO_{4+\delta}$ single crystals.** Solid State Ionics, 167 (3–4) (2004), pp. 341-347.

[22] E. Boehm, *et al.* **Oxygen diffusion and transport properties in non-stoichiometric $Ln_{2-x}NiO_{4+\delta}$ oxides.** Solid State Ionics, 176 (37–38) (2005), pp. 2717-2725.

[23] A. Tarancon, *et al.* **Layered perovskites as promising cathodes for intermediate temperature solid oxide fuel cells.** Journal of Materials Chemistry, 17 (30) (2007), pp. 3175-3181.

[24] A.A. Taskin, A.N. Lavrov, Y. Ando. **Achieving fast oxygen diffusion in perovskites by cation ordering.** Applied Physics Letters, 86 (2005), p. 091910.

[25] E. Boehm, *et al.* **Oxygen transport properties of $La_2Ni_{1-x}Cu_xO_{4+\delta}$ mixed conducting oxides.** Solid State Sciences, 5 (7) (2003), pp. 973-981.

[26] J. Dailly, *et al.* **Electrochemical properties of perovskite and A_2MO_4-type oxides used as cathodes in protonic ceramic half cells.** Journal of Solid State Electrochemistry, 15 (2) (2011), pp. 245-251.

[27] K. Takeuchi, *et al.* **The crystal structures and phase transitions in Y-doped $BaCeO_3$: their dependence on Y concentration and hydrogen doping.** Solid State Ionics, 138 (1–2) (2000), pp. 63-77.

[28] C. Allançon, *et al.* **Influence of oxygen on structural transitions in $Pr_2NiO_{4+\delta}$.** Solid State Ionics, 74 (3–4) (1994), pp. 239-248.

[29] S. McIntosh, *et al.* **Oxygen stoichiometry and chemical expansion of $Ba_{0.5}Sr_{0.5}Co_{0.8}Fe_{0.2}O_{3-\delta}$ measured by in situ neutron diffraction.** Chemistry of materials, 18 (8) (2006), pp. 2187-2193.

[30] R. Chiba, *et al.* **High temperature properties of $Ce_{1-x}Pr_xO_{2-\delta}$ as an active layer material for SOFC cathodes.** Solid State Ionics, 197 (1) (2011), pp. 42-48.

[31] Y.K. Chung, Y.-U. Kwon, S.H. Byeon. **Synthesis, structural and electrical characterizations of $Pr_{2-x}Ba_xNiO_{4+\delta}$.** Bulletin of the Korean Chemical Society, 16 (1995), pp. 120-125.

[32] W.D. Kingery, H.K. Bowen, D.R. Uhlmann. **Introduction to Ceramics.** John Wiley, New York (1976).

[33] L. Zhao, *et al.* **Reaction model for cathodes cooperated with oxygen-ion conductors for solid oxide fuel cells using proton-conducting electrolytes.** International Journal of Hydrogen Energy, 37 (1) (2012), pp. 548-554.

[34] C. Ferchaud, *et al.* **High performance praseodymium nickelate oxide cathode for low temperature solid oxide fuel cell.** Journal of Power Sources, 196 (4) (2011), pp. 1872-1879.

[35] S.B. Adler. **Reference Electrode Placement in Thin Solid Electrolytes.** Journal of The Electrochemical Society, 149 (5) (2002), pp. E166-E172.

[36] M. Cimenti, *et al.* **Distortions in Electrochemical Impedance Spectroscopy Measurements Using 3-Electrode Methods in SOFC. I–Effect of Cell Geometry.** Fuel Cells,, 7 (5) (2007), pp. 364-376.

[37] S.B. Adler, *et al.* **Reference electrode placement and seals in electrochemical oxygen generators.** Solid State Ionics, 134 (1–2) (2000), pp. 35-42.

[38] P. Dordor, *et al.* Phys. Appl., 20 (1985), p. 795.

[39] Laplume, J., *L'onde Electrique*. n° 335, 1955. 35: p. 114.

[40] J.M. Bassat, P. Odier, J.P. Loup. **The Semiconductor-to-Metal Transition in Question in $La_{2-x}NiO_{4+\delta}$ ($\delta > 0$ or $\delta < 0$).** Journal of Solid State Chemistry, 110 (1) (1994), pp. 124-135.

[41] F. Mauvy, *et al.* **Electrode properties of $Ln_2NiO_{4+\delta}$ (Ln = La, Nd, Pr): AC Impedance and DC Polarization Studies.** Journal of The Electrochemical Society, 153 (8) (2006), pp. A1547-A1553.

[42] G. Ma, T. Shimura, H. Iwahara. **Ionic conduction and nonstoichiometry in $Ba_xCe_{0.90}Y_{0.10}O_{3-\delta}$.** Solid State Ionics, 110 (1–2) (1998), pp. 103-110.

[43] W.G. Coors, D.W. Readey. **Proton Conductivity Measurements in Yttrium Barium Cerate by Impedance Spectroscopy.** Journal of the American Ceramic Society, 85 (11) (2002), pp. 2637-2640.

[44] M. Oishi, *et al.* **Defect structure analysis of B-site doped perovskite-type proton conducting oxide $BaCeO_3$: Part 2: The electrical conductivity and diffusion coefficient of $BaCe_{0.9}Y_{0.1}O_{3-\delta}$.** Solid State Ionics, 179 (39) (2008), pp. 2240-2247.

[45] E.J.L. Schouler, N. Mesbahi, G. Vitter. **In situ study of the sintering process of yttria stabilized zirconia by impedance spectroscopy.** Solid State Ionics, 9-10 (Part 2 (0)) (1983), pp. 989-996.

[46] A. Grimaud, *et al.* **Transport properties and in-situ Raman spectroscopy study of $BaCe_{0.9}Y_{0.1}O_{3-\delta}$ as a function of water partial pressures.** Solid State Ionics, 191 (1) (2011), pp. 24-31.

[47] E. Quarez, Y. Oumellal, O. Joubert. **Optimization of the Lanthanum Tungstate/Pr_2NiO_4 Half Cell for Application in Proton Conducting Solid Oxide Fuel Cells.** Fuel Cells, 13 (1) (2012), pp. 34-41.

[48] Y. Lin, R. Ran, Z. Shao. **Silver-modified $Ba_{0.5}Sr_{0.5}Co_{0.8}Fe_{0.2}O_{3-\delta}$ as cathodes for a proton conducting solid-oxide fuel cell.** International Journal of Hydrogen Energy, 35 (15) (2010), pp. 8281-8288.

[49] H. Uchida, S. Tanaka, H. Iwahara. **Polarization at Pt electrodes of a fuel cell with a high temperature-type proton conductive solid electrolyte.** Journal of Applied Electrochemistry, 15 (1) (1985), pp. 93-97.